On the Zonal Structure of the North Atlantic Oscillation and Annular Modes

EDWIN P. GERBER

Department of Applied Physics and Applied Mathematics, Columbia University, New York, New York

GEOFFREY K. VALLIS

GFDL, and Princeton University, Princeton, New Jersey

(Manuscript received 16 November 2007, in final form 15 July 2008)

ABSTRACT

The zonal structure and dynamics of the dipolar patterns of intraseasonal variability in the extratropical atmosphere—namely, the North Atlantic Oscillation (NAO) and the so-called annular modes of variability—are investigated in an idealized general circulation model. Particular attention is focused on the relationships linking the zonal structure of the stationary waves, synoptic variability (i.e., the storm tracks), and the zonal structure of the patterns of intraseasonal variability. Large-scale topography and diabatic anomalies are introduced to modify and concentrate the synoptic variability, establishing a recipe for a localized storm track. Comparison of the large-scale forcing, synoptic variability, and patterns of intraseasonal variability suggests a nonlinear relationship between the large-scale forcing and the variability. It is found that localized NAO-like patterns arise from the confluence of topographic and diabatic forcing and that the patterns are more localized than one would expect based on superposition of the responses to topography and thermal forcing alone.

The connection between the eddy life cycle of growth and decay and the localization of the intraseasonal variability is investigated. Both the termination of the storm track and the localization of the intraseasonal variability in the GCM depend on a difluent region of weak upper-level flow, where eddies break and dissipate rather than propagate energy forward through downstream development. The authors' interpretation suggests that the North Atlantic storm track and the NAO are two manifestations of the same phenomenon. Conclusions from the GCM study are critiqued by comparison with observations.

1. Introduction

What determines the zonal structure of the North Atlantic Oscillation (NAO) and the annular modes, the dominant patterns of variability in the extratropical atmosphere on intraseasonal time scales of 10–100 days? Various authors, including Limpasuvan and Hartmann (2000), DeWeaver and Nigam (2000), and Benedict et al. (2004) show or suggest that these large-scale patterns are driven and maintained by eddy–mean flow interactions and that their decorrelation time scale is on the order of 10–15 days (Feldstein 2000a, b). Relatedly, Vallis et al. (2004) and Cash et al. (2005) argue that the zonal spatial structure of these patterns is set by the underlying structure of the synoptic (2–10 day) variability. In the former study, zonally asymmetric synoptic variability is approximated in a barotropic model by a stochastic stirring that varies with longitude, whereas in the latter zonal asymmetries in the synoptic variability of an atmospheric GCM are created with topography and land–sea contrast. Despite these differences, however, the patterns of intraseasonal variability roughly follow the structure of the storm tracks in both models. If the storm tracks are statistically zonally uniform, so are the intraseasonal variability patterns: ideal annular modes. If the storm track is confined in longitude, so is the intraseasonal variability: the NAO. Jin et al. (2006) also attempt to provide a theoretical link between synoptic variability and low-frequency flow.

In this paper, we extend and critique this idealized interpretation of the large-scale variability as a response to eddy stirring. We investigate the interactions between synoptic and large-scale variability in a model of

Corresponding author address: Edwin P. Gerber, Courant Institute of Mathematical Sciences, New York University, New York, NY 10012.
E-mail: gerber@cims.nyu.edu

DOI: 10.1175/2008JAS2682.1

intermediate complexity relative to these earlier studies: a dry, primitive equation, atmospheric GCM. The model captures many aspects of that atmospheric flow with some fidelity, but simplifications of the forcing allow us to more easily control the large-scale climatology. We frame the study with respect to three questions:

1) What are the key features of the thermal and orographically induced stationary wave patterns that give rise to a synoptic storm track?
2) How does the life cycle of an eddy—or, rather, the evolution of an eddy wave packet—in a zonally varying flow relate to the large-scale variability?
3) How is the presence of a zonally localized storm track related to, or even the same as, the NAO?

In trying to answer these questions, we seek to understand the zonal structure of the NAO and annular modes.

To first order, localized storm tracks follow from the localization of the large-scale baroclinicity in stationary wave patterns created by orography and thermal forcing. Localization of the baroclinicity (described, for example, by Pierrehumbert 1984), however, is not necessarily sufficient to create a localized storm track, and because of downstream development the storm tracks do not necessarily coincide with the regions of maximum baroclinicity (Chang and Orlanski 1993; Swanson 2007). Furthermore, the patterns of variability (as described, for example, by teleconnections and empirical orthogonal functions) do not perfectly correspond to the storm tracks, although some connection is apparent. Our overall goal is to better understand the relationships among all these patterns, although we are not wholly successful.

Following a description of our model in section 2, we explore the response of planetary stationary waves and the patterns of intraseasonal variability to various topographic and thermal forcings in section 3. The perturbations are introduced to break the zonal symmetry of the model and approximate the effect of the Rocky Mountains and land–sea contrast between North America and the Atlantic Ocean in winter. Although we find the stationary wave pattern to be a roughly linear function of the topography and thermal forcing, the storm tracks and the associated patterns of variability are not, and this is explored in section 4. We find that the termination of the storm track by a weak region of upper-level flow is key to producing the localized storm track in our model, as anticipated by Lee (1995), Whitaker and Dole (1995), and Swanson et al. (1997). The role of eddy–mean flow interactions and the evolution of individual eddies and wave packets is further explored in section 5. Using the eddy life cycle of Simmons and Hoskins (1978) as a guide, we show that it is the end or ''death'' of the storm track, where decaying eddies deposit momentum in the flow, that is most vital for the creation of coherent shifts in the jet.

In section 6, we critique the picture that emerges from our idealized GCM in view of the observed storm tracks. Finally, in section 7, we present an alternative strategy for characterizing changes in the extratropical jet based on the number of distinct jets in the flow. This scheme provides comparable information about the extratropical circulation as EOF analysis, but it suggests a physical interpretation of the NAO as the interaction of two one-dimensional vortex pairs (two jets), merging and separating. Our results and conclusions are summarized in section 8.

2. Procedures and model setup

We use the GFDL dry dynamical core, a sigma ($\sigma = p/p_s$) coordinate spectral model of the primitive equations on the sphere, with a simplified forcing similar to that described by Held and Suarez (1994, hereafter HS94). The chief simplification is in the temperature equation; in lieu of radiation and convection schemes, Newtonian relaxation to a prescribed temperature profile T_{eq} is applied:

$$\frac{DT}{Dt} = \ldots - k_a\left[T - T_{\text{eq}}(\lambda, \phi, p)\right]. \tag{2.1}$$

The equilibrium profile approximates a state of radiative–convective equilibrium, with near-zero stability in the vertical and steep horizontal temperature gradients from equator to pole. In the standard HS94 configuration, T_{eq} is zonally uniform. The damping k_a is almost everywhere set to $(40\ \text{day})^{-1}$, the exception being in the low-level tropics, where it is increased to $(4\ \text{day})^{-1}$ at the surface to give the model a more realistic Hadley circulation. Momentum is removed from the model near the surface by a Rayleigh drag. The drag at the surface is set by $k_f = 1\ \text{day}^{-1}$ and decreases linearly to the $\sigma_0 = 0.7$ surface, where it vanishes. A ∇^8 damping is included to remove enstrophy at small scales. The damping time on the smallest resolved scale is 1/10 of a day.

The zonal symmetry of the HS94 forcing is broken by the addition of Gaussian topography and perturbations to equilibrium temperature profile. We experimented with mountains of varying shape and height and found the results to be relatively robust provided the topography is positioned so as to block the extratropical jet. In the integrations described here we use a ridge comparable in horizontal scale to the Rocky or Andes Mountains. The ridge is 40° long in latitude and centered at 40°N. It tapers off with a half-width of 12.5° at either end

so that it does not extend into the Southern Hemisphere. The half-width of the ridge in longitude is 12.5°. The height of the ridge h_0 was varied from 0 (no topography) to 3000 m in 1000-m increments. In almost all integrations the ridge is centered in longitude at $\lambda_0 = 90°$W. It was changed to $\lambda_0 = 60°$ in one additional integration to test the sensitivity of the variability to the relative position between the topographic and diabatic forcings.

We approximate diabatic effects associated with the land–sea contrast by adding a high-latitude region of cooling (i.e., a continent) and warming (i.e., an ocean) with a sharp change between them, as is seen on the eastern coasts of Asia and North America. The cooling at high latitudes increases the temperature gradient to the south, creating a zonally localized baroclinic zone, whereas the high-latitude heating reduces the gradient, producing a weak baroclinic zone. The details of the perturbation are discussed in the appendix of Gerber and Vallis (2007). The heating/cooling is strongest at the surface and decays to zero at the tropopause. We quantify the strength of the diabatic perturbation by the maximum heating rate a_0. It was varied from 0 (no heating) to $\pm$ 4 K day^{-1}. These heating rates are somewhat large but are of the same order as those observed in Hoskins and Valdes (1990).

TABLE 1. Integration specifications. The parameters h_0, λ_0, and a_0 quantify the height and location of the topography and maximum strength of the heating/cooling anomalies, respectively. For reference, the boundary between the cold and warm anomalies is located at the prime meridian and always positioned at 6 o'clock in figures. We focus on four of the integrations in particular and have given them more descriptive names: RM (Rocky Mountains) for integration 3 with just topography, LSC (land–sea contrast) for integration 9 with just thermal forcing, LSC+RM for integration 11 with both topographic and thermal forcing, and LSC+RM2 for integration 13.

Integration	Topography		Thermal forcing
	h_0 (m)	λ_0	a_0 (K day^{-1})
1	0	—	0
2	1000	90°W	0
3 (RM)	2000	90°W	0
4	3000	90°W	0
5	0	—	2
6	1000	90°W	2
7	2000	90°W	2
8	3000	90°W	2
9 (LSC)	0	—	4
10	1000	90°W	4
11 (LSC+RM)	2000	90°W	4
12	3000	90°W	4
13 (LSC+RM2)	2000	60°W	4

a. Simulation specifications

The model was run with triangular truncation at wavenumber-42 resolution with 20 evenly spaced σ levels in the vertical. The temporal variability of the model is known to be sensitive to resolution (Gerber et al. 2008), but the behavior at this resolution appears to be robust. The data were sampled daily for 9000 days (approximately 25 yr) after an initial spin up period of 250 days. We present results from the 13 integrations listed in Table 1.[1] In the first 12 integrations the amplitude of the topography and diabatic forcing are systematically varied. The optimum alignment between the topographic and heating anomalies (in terms of the baroclinicity, as detailed later in the text) was used for this set. Integration 13 is a variation of integration 11, in which the mountain has been shifted 30° to the east. In our analysis we focus on four of the integrations in particular, and have given them more descriptive names: RM (Rocky Mountains) for integration 3 with only realistic scale topography, LSC (land–sea contrast) for integration 9 with only a thermal perturbation, LSC+RM for integration 11 with both topographic and thermal forcing, and LSC+RM2 for integration 13.

b. Analysis techniques

Computations from model data were completed on the native σ coordinates and the results were interpolated to pressure surfaces when appropriate. High-pass statistics were computed with a Lanczos filter with cutoff frequency $f_c = 10^{-1}$, thereby capturing frequencies between roughly (2 days)$^{-1}$ and (10 days)$^{-1}$. A digital window of $2n+1=41$ provides sufficient breadth for a clean frequency cutoff (Duchon 1979).

The intraseasonal variability is characterized by the first empirical orthogonal function of the 25-day averaged sea level pressure (SLP). The bias due to the decrease in separation of grid points at high latitudes is corrected by weighting fields with a factor of $\cos^{1/2}\phi$, and all EOFs shown in this paper are statistically robust according the "rule of thumb" proposed by North et al. (1982). We considered the effect of averaging the SLP in time on the EOF patterns because the choice of averaging can affect the spatial structure of the observed Northern Hemisphere annular mode (NAM; Woollings and Hoskins 2008). In our model, however, we find almost no sensitivity in the spatial patterns. (When the averaging is increased, the top EOF does, however, explain a larger fraction of the remaining variance. This is because the top EOFs have more power at lower frequencies relative to higher-order modes and so become more pronounced as one focuses on lower frequencies.) We refer to the first EOF pattern as the northern annular mode of the integration, recognizing that it is probably not a linear mode of the system. Daily annular mode time series, the "NAM indices," were

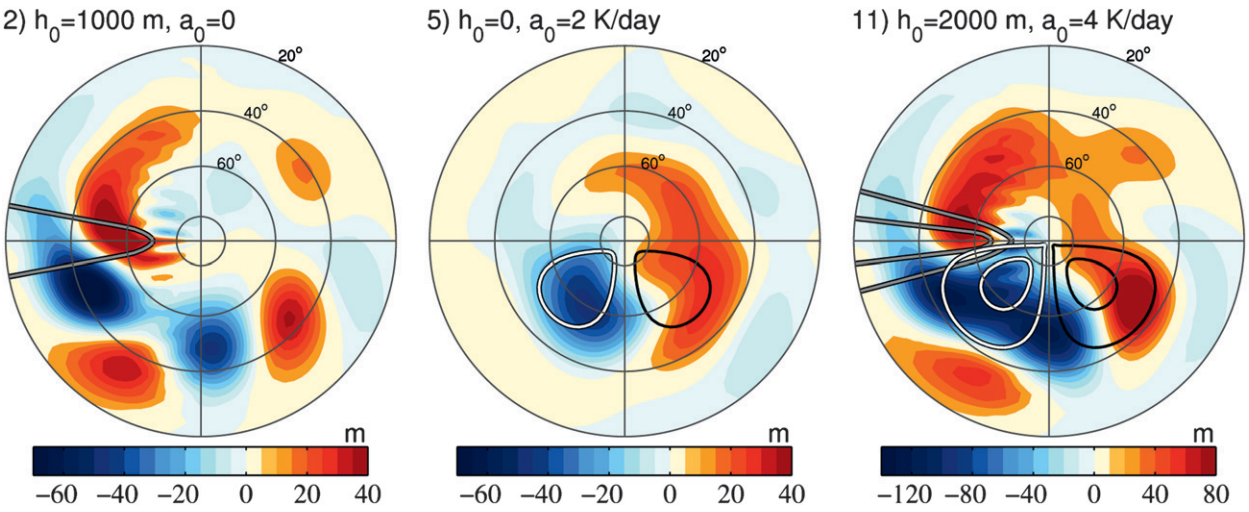

FIG. 1. The standing wave $\bar{z}*$ at 500 hPa for integrations 2 (small topography alone), 5 (weak diabatic forcing alone), and 11 (moderate topography and thermal forcing). The cooling and heating regions are marked by thick white and black contours, respectively. The contours mark the perturbation to the equilibrium temperature profile and roughly correspond to regions with cooling/heating rates of ± 1 and 3 K day^{-1}. The thick gray lines show the location of the topography, and mark the 500-m, 1500-m, 2500-m, ... contours. These conventions will be used in following figures.

computed by projecting the daily SLP anomalies onto the EOF pattern and were standardized to have unit variance.

3. Nonlinear localization of the intraseasonal variability: The NAO

What controls the zonal structure of the northern annular modes or, likewise, the zonal localization of the North Atlantic Oscillation? To compare the impact of the topographic and thermal forcings, we first focus on a common metric, the stationary wave response to the perturbations. The standing wave $\bar{z}^* = \bar{z} - [\bar{z}]$ at 500 hPa is shown for integrations 2, 5, and 11 in Fig. 1. Here and throughout the text, an overbar refers to the time average and a prime indicates deviations from the time average; similarly, square brackets refer to the zonal average, and an asterisk indicates deviations from the zonal average. Integrations 2 and 5 have weak topographic ($h_0 = 1000$ m) and thermal forcing ($a_0 = 2$ K day^{-1}), respectively, and so exhibit the most linear response to the zonally asymmetric perturbations. The topography is outlined by the thick gray lines and the cooling and warming anomalies by white and black lines, respectively. The structure of the response to topography alone (on the left), is in keeping with that suggested by one-layer quasigeostrophic (QG) theory (e.g., Vallis 2006, chapter 13). A standing wave forms 1/4 of a wavelength out of phase with the topography, with a ridge upstream and a trough immediately downstream. With thermal forcing (middle panel), the response is more confined to the high latitudes. A low develops slightly downstream of the cooling anomaly and a high develops downstream of the warming anomaly.

The topography and thermal perturbations were aligned to localize the baroclinicity of the flow (and thus create a storm track) in integration 11, shown in the right panel. Here the low- and high-pressure anomalies from the topography and thermal forcing increase the strength of the jet stream in the quadrant between 90°W and the prime meridian. Note that the contour interval has been doubled to plot the stationary wave response to integration 11, which is forced with a mountain twice as large as in integration 2, and a diabatic perturbation twice as strong as in integration 5. *The stationary wave response to diabatic and thermal perturbation appears to be roughly additive,* that is, the standing wave generated by a 2000-m ridge and 4 K day^{-1} heating is roughly equal to the sum of 2 times the response to a 1000-m ridge and 2 times the response to 2 K day^{-1} heating.

The stationary wave response to topographic and diabatic forcing is linear in this additive sense for all integrations, as demonstrated in Table 2. Here we show that the spatial structure and amplitude of the standing waves at 500 hPa in integrations 2–12 can be well predicted from the response in integrations 2 and 5 alone. Specifically, we compare the spatial correlation and root-mean-square (RMS) amplitude of the stationary wave observed in each integration to that given by the appropriate linear combination of the waves in integrations 2 and 5. The table is best explained by example.

TABLE 2. Linearity of the stationary wave response to topographic and thermal forcing. The rows (columns) specify the strength of the thermal (topographic) forcing of the integration. For each combination of topographic and thermal perturbations, we compare the standing wave at 500 hPa with that constructed from integrations 2 (1000-m topography, no heating) and 5 (2 K day^{-1} heating, no topography), assuming the linear relationship as described in the text. The first number is the square of the pattern correlation coefficient R^2 and reflects the fraction of the observed pattern that is linearly congruent with the linear combination. The second number, in parentheses, is the ratio of the RMS amplitude of the observed pattern to the linear combination; values less than 1 imply that the observed pattern is smaller in amplitude than would be expected if the stationary wave response were purely additive. Uniformly high pattern correlation and amplitude ratios near 1 suggest that the stationary wave response to topographic and thermal perturbations is fairly linear. From left to right, the first row contains information for integrations 1, 2, 3, and 4, the second for integrations 5, 6, 7, and 8, and the third, integrations 9, 10, 11, and 12.

	Topographic amplitude h_0 (m)			
Thermal forcing a_0	0	1000	2000	3000
0	—	1(1)	0.84(0.80)	0.69(0.69)
2 K day^{-1}	1(1)	0.91(0.98)	0.90(0.91)	0.78(0.82)
4 K day^{-1}	0.92(0.87)	0.87(0.83)	0.90(0.92)	0.80(0.90)

The entries in the box in the third row (4 K day^{-1}) and third column (2000 m) compare the standing wave $\bar{z}^*_{11}$ in the simulation with these perturbations, in this case integration 11, to the relevant linear combination of the standing waves from integrations 2 and 5, in this case $2\bar{z}^*_2+2\bar{z}^*_5$. The first entry, 0.90, is the square of the spatial correlation coefficient R^2 between the patterns, and so indicates the fraction of the pattern $\bar{z}^*_{11}$ that is linearly congruent with $2\bar{z}^*_2+2\bar{z}^*_5$. The second entry, (0.91), is the ratio of the RMS amplitude of $\bar{z}^*_{11}$ to that of $2\bar{z}^*_2+2\bar{z}^*_5$. Thus, the standing wave in integration 11 is 91% as large as one would expect from a weighted sum of the components.

With the exception of integration 4, the R^2 pattern correlation values indicate that roughly 80% or better of the spatial structure of the stationary wave response can be predicted from a simple linear combination of the waves generated by the components. The linear combinations also predict the amplitude of the response fairly well. In general, the observed waves are slightly weaker (10%–20%) in amplitude than those suggested by the linear combinations. Nonlinearity appears to be most important in integration 4, where the amplitude of the response is only twice as large as in integration 2, despite the fact that the mountain is 3 times larger. Even here, however, almost 70% of the structure and amplitude is captured by a simple linear combination.

Having established that the response of the stationary waves to topography and thermal perturbations is roughly additive, we turn to the patterns of intraseasonal variability. Figure 2 illustrates the northern annular mode computed from each of the 13 model integrations. Quick inspection of the figure suggests that *the EOF patterns do not share the linear additive property of the stationary wave response*. Most of the EOF patterns are fairly annular in structure. It is only with a combination of both thermal and topographic forcing, in particular integrations 8, 11, and 12, that we see significant localization of the intraseasonal variability: these patterns more closely resemble the NAO. The key features that distinguish these integrations are significant localization of the equatorward lobe of the EOF between 0° and 90°E and the offset of the polar lobe away from the pole. With topographic forcing alone (integrations 2, 3, and 4), the EOF patterns are fairly annular, modified only by a wavenumber-5 perturbation. Integrations with just thermal forcing (5 and 9) reveal some localization of the NAM east of the prime meridian, but the polar lobe of the EOF is still over the pole.

We first note that the zonally averaged structure of the NAM patterns is the same in all integrations despite significant changes in the zonal distribution of the modes. The pattern correlation R^2 of the zonal average of the NAM from the integrations with zonal asymmetries (2–13) with that of the control integration (1) is above 0.95 in all cases. The amplitude of the zonally average response is also nearly uniform, with the exception of integrations 1, 5, and 9, where the strength of the dipole is roughly 30% larger. This implies that in all integrations with some topographic forcing, the total oscillation in mass between high and midlatitudes is the same despite significant changes in the distribution of the oscillation (i.e., compare the NAM in integration 2 to that of integration 12). The fact that net distribution of mass is larger in integrations 1, 5, and 9 is significant, and it is likely the impact of increased eddy–mean flow interaction in the absence of topography, as diagnosed by Gerber and Vallis (2007).

We next focus on the nonzonal structure of the NAM patterns. To quantify the linearity (or lack thereof) in the response to topographic and diabatic thermal forcing, we repeat the analysis in Table 2, but now with the nonzonal component of the EOF patterns. In Table 3 we ask this question: how much of the zonally asymmetric structure and amplitude of the observed NAM patterns can be predicted from the NAM patterns of integrations 2 and 5, with weak topographic and diabatic forcing, respectively? For integrations with more annular NAM patterns (3, 6, 7, 9, and 10) the pattern correlation values suggest that only about half of the nonzonal EOF structure can be captured from a linear

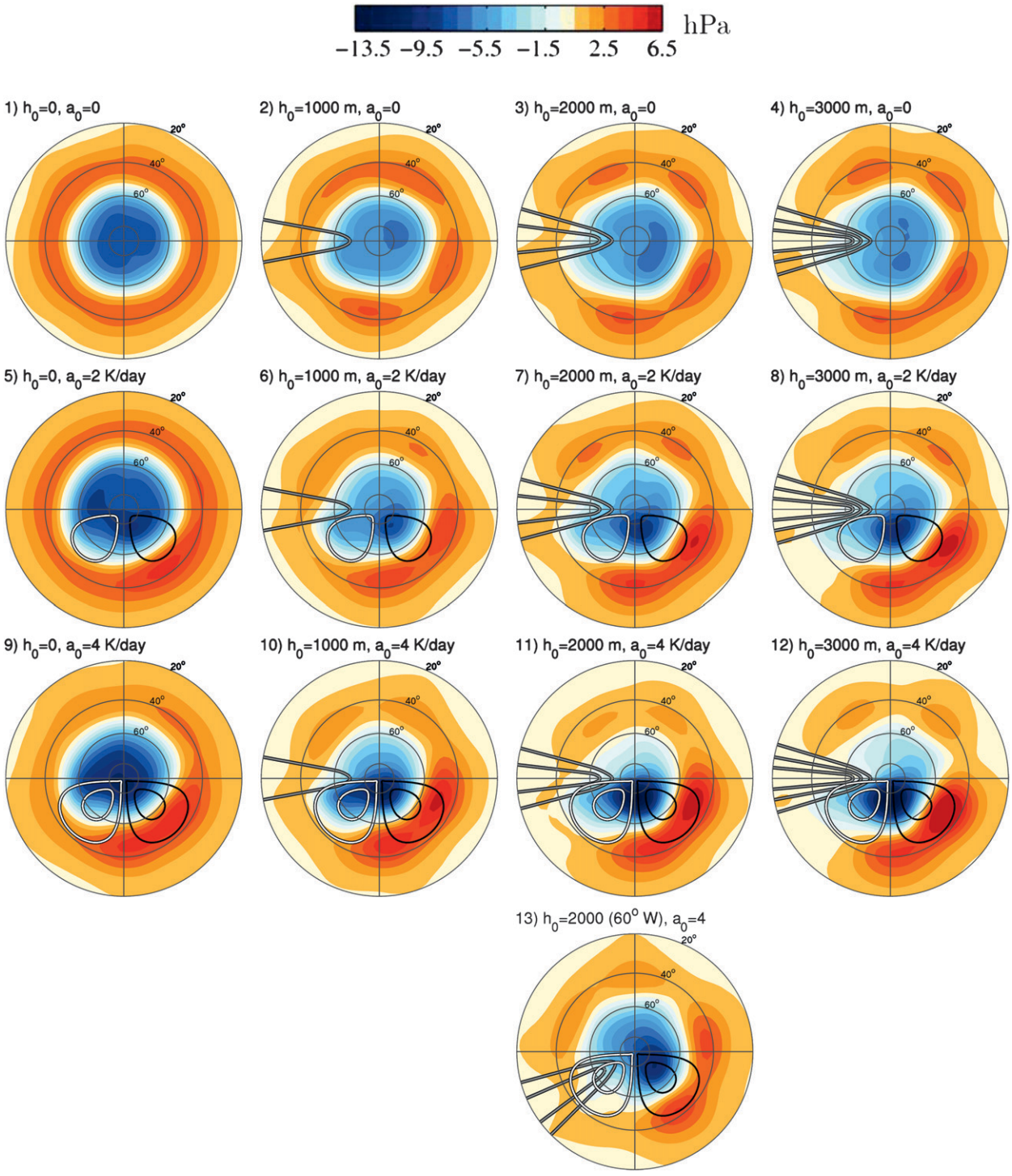

FIG. 2. The northern annular mode computed from each integration. The NAM here is defined as the first EOF of the 25-day averaged sea level pressure. The patterns are given in units of hPa by regressing daily surface pressure anomalies on the standardized annular mode indices (see section 2) and thus have magnitudes corresponding to a one standard deviation, positive phase event.

combination of the components. With the NAO-like integrations 8 (h_0 = 3000 m, a_0 = 2 K day^{-1}), 11 (h_0 = 2000 m, a_0 = 4 K day^{-1}) and 12 (h_0 = 3000 m, a_0 = 4 K day^{-1}), however, the pattern correlation is extremely low; only about one quarter of the structure is consistent with the linear combination of the components. In

TABLE 3. Linearity of the NAM response to topographic and thermal perturbations. The values are the same as in Table 2 but are based on the nonzonal components of the NAM patterns of variability. The response of the intraseasonal variability to perturbations is decidedly less linear than the response of the standing waves. The low pattern correlation R^2 values (particularly for integrations 4, 8, 11, and 12) suggest that there is almost no skill in predicting the zonally asymmetric structure of the NAM given the NAM patterns of integrations 2 and 5 with weak topographic and thermal perturbations, respectively.

	Topographic amplitude h_0 (m)			
Thermal forcing a_0	0	1000	2000	3000
0	—	1(1)	0.52(0.68)	0.32(0.53)
2 K day^{-1}	1(1)	0.57(0.86)	0.50(0.85)	0.33(0.73)
4 K day^{-1}	0.81(0.88)	0.54(0.86)	0.20(0.95)	0.18(0.84)

other words, knowledge of the EOF response to topography or thermal forcing alone provides almost no skill in predicting the response to the combined forcing. This is stark contrast to the standing waves.

The total amplitude of the zonally asymmetric structure does seem to scale more linearly. With the exception of the topography-only runs (3 and 4), the RMS amplitude of the zonal asymmetries in the EOF scale linearly with that suggested by the components. This is particularly true in integration 11, where the relative amplitude of the zonal asymmetries in the NAM is 95% of that suggested by a simple linear combination.

To determine the importance of the relative location of the topography and thermal forcings, we seek another, more flexible measure of the (non)linearity in the NAM response. Focusing now on just integrations 11 and 13, we ask another question: how well can one construct the NAM in these integrations as a linear combination of the patterns of variability in the integrations with just topography or diabatic forcing? We define a linear combination $\mathrm{NAM}_{\alpha,\beta}$ of the NAM patterns from integrations 9 (just thermal forcing) and 3 (just topography),

$$\mathrm{NAM}_{\alpha,\beta}(\lambda,\phi) = \alpha\mathrm{NAM}_9(\lambda,\phi) + \beta\mathrm{NAM}_3(\lambda,\phi), \quad (3.1)$$

for positive scalars α and β. (We use integrations 3 and 9, as opposed to 2 and 5, to avoid the nonlinearity associated with the amplitude of the topography/thermal perturbations, thus optimizing our chance for a good fit.) In Figs. 3a and 3b we show that the best linear combination $\mathrm{NAM}_{\alpha,\beta}$ fits to the NAM of integrations 11 and 13, respectively. The best fits are obtained by minimizing the RMS latitude-weighted difference between the linear combination $\mathrm{NAM}_{\alpha,\beta}$ and the observed NAM patterns over all α and β. For integration 11, the minimizing coefficients are $\alpha_0 = 0.30$ and $\beta_0 = 0.52$. For integration 13, the best fit is further biased toward the topography-only NAM, $\alpha_0 = 0.16$ and $\beta_0 = 0.81$; here, of course, we offset the pattern associated with the topography (integration 3) by 30° for a fair comparison.

The bottom panels of Fig. 3 show the error between the best fit linear combination and the actual NAM patterns for integrations 11 and 13. The RMS error is over twice as great for the reconstruction of the NAM in integration 11 as for that of integration 13; in the former, the relative error is 59%, whereas in the latter the relative error is a more reasonable 28%. There is a systematic bias in the error in the reconstruction of NAM_{11} at both high and midlatitudes: the NAM of this simulation is much more localized than in the integrations with topography or thermal forcing alone.

In summary, the pattern correlation statistics and best fit linear combinations suggest that the non-zonal component of the NAM patterns is quite sensitive to the details of the thermal and topographic forcings and do not scale linearly like the standing wave response. Our integrations indicate that nonlinear interactions between the topographic and thermally induced zonal perturbations are important in the zonal localization of the variability. NAO-like variability is only found when topographic and thermal forcings are combined, and then only when they are aligned properly. Given the importance of this nonlinearity, it is quite remarkable that the zonal average signature of the NAM is so insensitive to the zonally asymmetric perturbations. To stress this point, the total oscillation in mass in integrations 7, 11, and 12, with a highly zonally localized NAM patterns, is the same as that in, say, integration 2, with a near perfectly symmetric structure. The exception to this rule is the integrations with no zonal asymmetries. Here zonal–mean flow feedback increases the overall strength of the NAM pattern by approximately 30%.

For the remainder of this study, we seek to understand the dynamics behind the nonlinear increase in zonal asymmetry in the NAM pattern that leads to NAO-like variability. We focus on four integrations in particular that capture the features in the set as a whole. Integration 3 captures the features of the response to topography alone (2, 3, and 4), and will be denoted by the more intuitive name RM for Rocky Mountains. Integration 9 captures the response to thermal perturbations alone (5 and 9) and will be denoted LSC for land–sea contrast. Integration 11 captures the highly localized NAO-like variability seen in integrations 8, 11, and 12, and will be denoted LSC+RM. The weak nonlinearity of the response to topography and thermal perturbations in 6, 7, and 10 falls in between these integrations. Integration 13 will be denoted LSC+RM2 and used to highlight the need for optimal alignment.

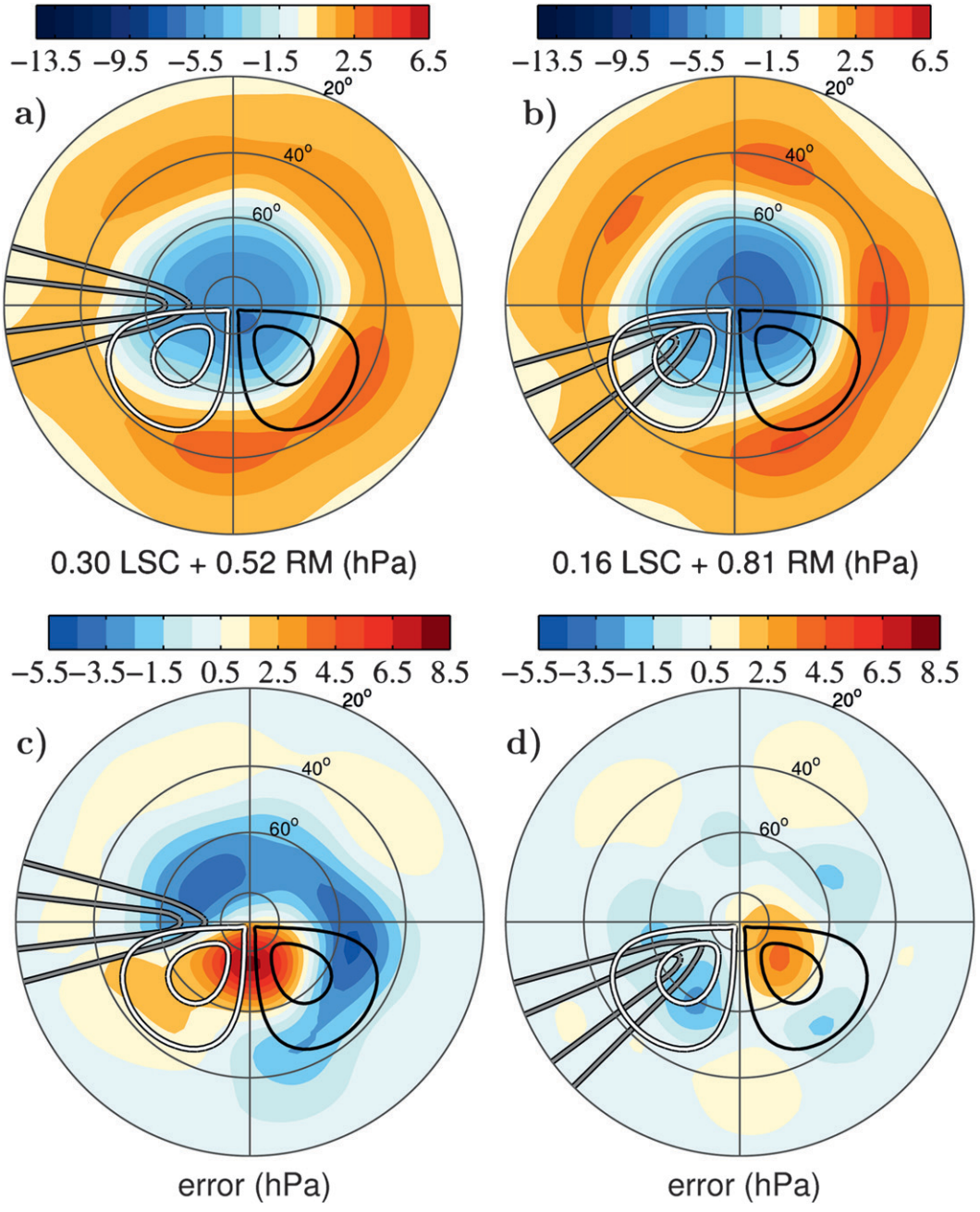

FIG. 3. Illustration of the nonlinearity in the NAM response. (a), (b) The best fit linear reconstructions of the NAM of integrations 11 and 13, respectively; (c),(d) the error in the reconstructions, NAM(α_0, β_0) − NAM_{11} and NAM_{13}, respectively.

4. The relationship between the storm track and the NAM

Based on the findings of Vallis et al. (2004) and Cash et al. (2005), we expect localization of the NAM to be connected to zonal localization of eddy kinetic energy (EKE) in a storm track. We begin by analyzing the impact of the thermal and topographic perturbations on the storm tracks in isolation before looking at their combined impact. The thermal perturbation designed to mimic land–sea contrast in integration LSC produces a moderately zonally localized storm track, as shown in Fig. 4. The baroclinicity of the flow is quantified by the Eady growth parameter

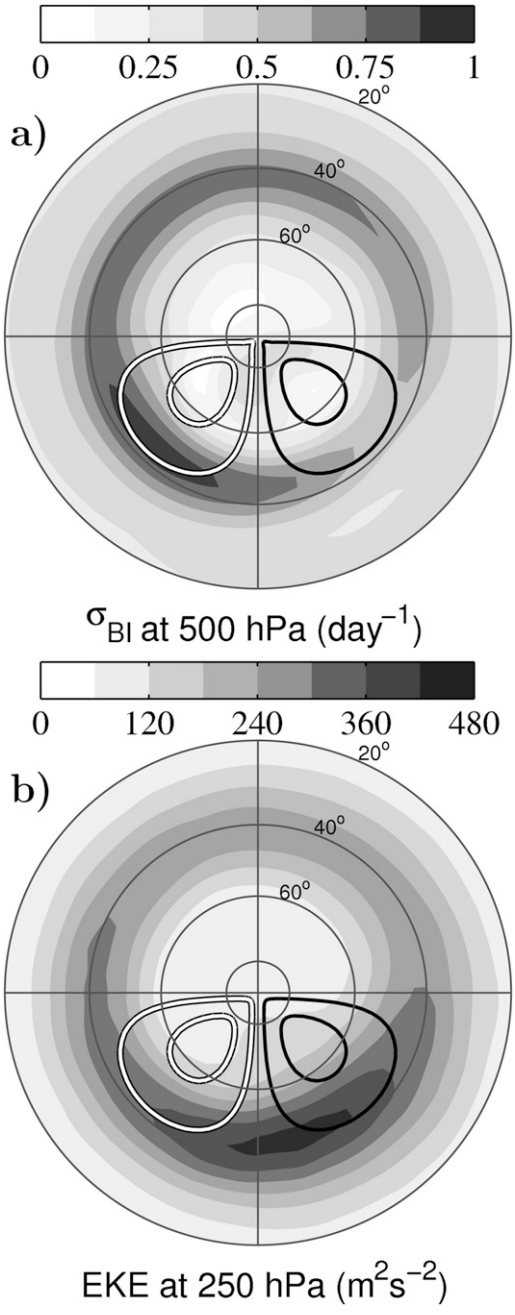

FIG. 4. (a) The Eady growth rate $\sigma_{\rm BI}$ at 500 hPa and (b) the eddy kinetic energy K_e at 250 hPa in integration LSC. We find that the Eady growth rate at this midlevel faithfully represents features of the baroclinicity through the lower and midtroposphere. The K_e is plotted in the upper troposphere where eddy amplitudes are greatest.

$$\sigma_{\rm BI} = 0.31 f \left| \frac{\partial \bar{\mathbf{V}}}{\partial z} \right| N^{-1} \tag{4.1}$$

at 500 hPa, where f is the Coriolis parameter, $\mathbf{V} = (u, v)$ the time-averaged two-dimensional wind vector, and N the Brunt–Väisälä frequency. The peak in baroclinicity

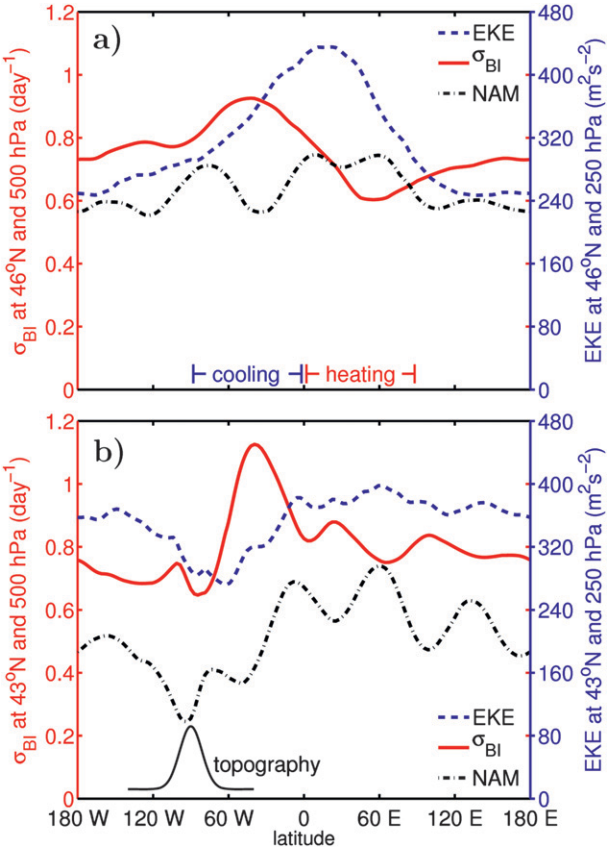

FIG. 5. The relationship between the baroclinicity of the flow, the storm tracks, and the NAM for integrations (a) LSC and (b) RM. The solid red curves characterize the stability of the flow, showing the Eady growth rate $\sigma_{\rm BI}$ as a function of longitude, and correspond with the left axes. The localization of the storm track is quantified by plotting the eddy kinetic energy (dashed blue curves, corresponding to the right axes). The longitudinal profiles of $\sigma_{\rm BI}$ and the EKE are taken at the latitude where the respective quantity is maximal. The zonal structure of the NAM is shown by the dotted–dashed curve, which provides a relative measure of the strength of the pattern at different longitudes, and is discussed in the appendix. The locations of the heating, cooling, and topographic perturbations are shown for reference.

is slightly equatorward of the the peak cooling anomaly (denoted by the thick white contours). The transient eddy kinetic energy, $K_e = \overline{(u'^2 + v'^2)}/2$, is shown in the left panel; it peaks approximately 60° downstream of the baroclinic maximum.

The relationship between the baroclinicity and the storm track in Fig. 4 can be summarized in one figure by considering slices of the baroclinicity and EKE along one line of latitude, as shown in Fig. 5a by the solid red and dashed blue lines, respectively. The same statistics, but for integration RM, where the only zonal asymmetry is a ridge comparable in size to the Rocky Mountains, are shown in Fig. 5b. The standing wave generated by the topography produces variations in the baroclinic

growth rate, and the peak in σ_{BI} is located approximate 50° downstream of the ridge. The relative difference between the minimum and maximum in the baroclinicity in RM is comparable to that in LSC (varying from 0.7 to 1.15 day^{-1} in RM and 0.6 to 0.9 day^{-1} in LSC), but there is almost no localization of the eddy kinetic energy except for a small dip immediately downstream of the topography.

Why is the eddy kinetic energy much more localized in integration LSC as compared to RM? Localization of the baroclinic growth requires the flow to be sufficiently unstable at the baroclinic maximum that the local eddy growth tendency is strong enough to compensate for the fact that the eddies are continually being advected downstream (Pierrehumbert 1984). There must also be sufficient contrast in the baroclinicity around the latitude circle for the local maximum to stand out. In our model, however, the peak baroclinicity in RM is greater than in LSC, as is the contrast between the maximum and minimum in growth rates. This would seemingly favor greater localization in integration RM and suggests that other effects are also important. Chang and Orlanski (1993) show that localization of the eddy energy also depends on the balance between downstream development and local barotropic energy conversion. Ageostrophic geopotential height fluxes tend to flux eddy energy downstream within wave packets. In a channel model, they found that this tendency was sufficient to even out the EKE despite large changes in the baroclinic growth rates. They argue that the variations in frictional damping over land and sea may prevent the downstream flux of eddy energy and thus localize the storm tracks in the atmosphere. This mechanism, however, cannot explain the differences in our model, where the surface friction is everywhere the same.

Swanson et al. (1997) argue that zonal variations in the upper tropospheric time-mean flow can modulate the structure and amplitude of eddies and thus produce a zonally localized storm track. They model upper tropospheric eddies as contour waves and find that both nonlinear wave breaking and the irreversible loss of wave energy increase in regions where contours separate. This suggests that difluent regions with weak upper-level flow prevent eddy energy from propagating downstream and so kill the storm track, leading to a zonally localized maximum in EKE downstream from the baroclinic maximum.

Linear theory states that the perturbation amplitude of a wave η is inversely proportional to its phase speed relative to the mean flow. That is,

$$\eta \propto \frac{\psi}{\bar{u} - c}, \tag{4.2}$$

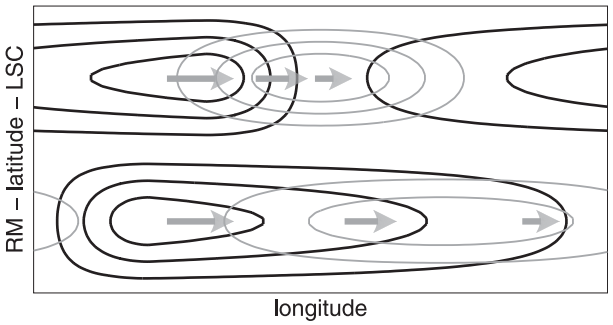

FIG. 6. A diagram illustrating the key differences in the structure of the baroclinicity and storm tracks of simulations (upper half) LSC and (lower half) RM. Thick black contours denote the baroclinicity and thus the upper-level winds; thin gray contours indicate the EKE and the arrows indicate the flux of the EKE, which is dominated by advection and downstream ageostrophic geopotential height fluxes. The EKE becomes localized where there is convergence of eddy kinetic energy fluxes. In LSC, this occurs in the weak baroclinic region immediately downstream of the baroclinicity maximum. In RM, downstream EKE fluxes compensate for the changes in baroclinic growth, and the EKE created in the baroclinic region is slowly deposited around the latitude circle.

where ψ is the perturbation streamfunction and c the phase speed of the wave. Wave displacements increase as the phase speed of the flow approaches that of the wave, thus increasing the importance of nonlinear effects. Rossby waves can only exist when $\bar{u} > c$, so the carrying capacity of the jet is linked to the speed of the jet. If we naively assume that all phase speeds are equally excited in the baroclinic region, the number of waves that become nonlinear (and either break or dissipate) is proportional to $-\partial u/\partial x$. Thus, in regions of decreasing upper-level flow energy converges rather than propagating downstream, and we expect increased eddy kinetic energy. The magnitude of σ_{BI} can be viewed as a proxy for the upper-level flow because its calculation is dominated by the vertical wind shear and the surface winds are weak. Consistent with the heuristic above, we find the greatest K_e in the region where the baroclinicity (upper-level wind) is decreasing in Fig. 5a.

The localization of eddy kinetic energy can be viewed as a balance between sources and sinks of eddy energy and advection by the mean flow. The difference in the longitudinal structure of the upper-level flow between integrations LSC and RM is illustrated in the diagram in Fig. 6. The slow increase in upper-level winds followed by the sharp decrease in LSC produces a more localized storm track: a peak in baroclinicity injects eddy energy just upstream of a difluent region, where eddies are sheared out and cannot propagate energy forward, leading to rapid convergence of eddy activity. The slower decay in the baroclinicity in RM allows eddy energy to propagate forward through downstream

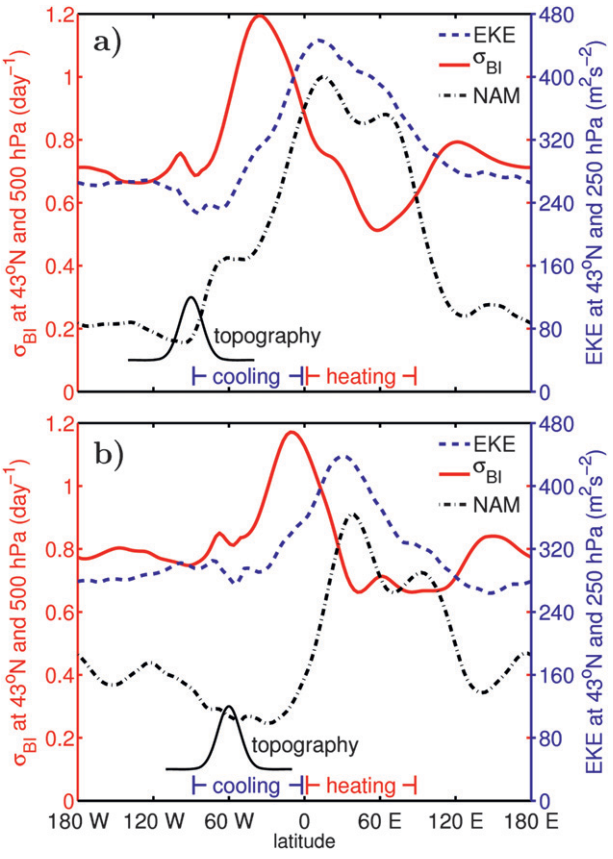

FIG. 7. As in Fig. 5, but for integrations with both diabatic and topographic forcing: (a) LSC+RM and (b) LSC+RM2.

development. The integrations suggest that a zonally localized storm track depends on both a ''growth'' region of strong instability to generated eddy energy and a ''death'' region that prevents eddies from continuing downstream.

The impacts of both topography and the thermal forcing are explored in integrations LSC+RM and LSC+RM2 and illustrated in Fig. 7. In integration LSC+RM, the topography and thermal perturbations were aligned to maximize the baroclinicity near 45°W. In LSC+RM2 the mountain was placed over the cold continent, to appear more consistent with the position of the Rocky Mountains relative to the Atlantic Ocean. The standing wave generated by the topography, however, dominates that generated by the thermal perturbation. Thus, the baroclinic maximum is about the same in two integrations. The two integrations differ significantly in the exit region of the storm track; the stronger dip in baroclinicity observed near 60°E in LSC+RM is absent in LSC+RM2. Because the baroclinicity can be viewed as a proxy for the upper-level winds, we find that LSC+RM better captures the difluent region over the Atlantic and is thus more representative of the observed flow.

Both integrations exhibit stronger localization of the baroclinicity than LSC or RM, but the peak-to-trough amplitude of the eddy kinetic energy is not much larger than in integration LSC. In fact, the storm track in LSC+RM2 is actually a bit weaker by this measure. The peak in K_e is more tightly constrained in longitude, however, particularly in integration LSC+RM. The localized storm track is found in the region where the baroclinicity (and hence the upper-level flow) is weakening: EKE is maximum in regions where $\partial u/\partial x$ is negative. The better storm track in LSC+RM relative to LSC+RM2 supports the argument that a difluent region is most important for localizing the synoptic variability.

The black dotted–dashed curves in Figs. 5 and 7 show the zonal structure of the NAM in these four integrations. Comparison of the storm tracks (EKE) and NAM in these integrations suggests that the zonal structure of the NAM does not necessarily follow that of the storm track. Such an argument works reasonably well for integrations LSC+RM and LSC+RM2; if anything, the localization of the NAM is exaggerated relative to the storm track in these integrations. In LSC, however, there is a zonally localized storm track, but the NAM is almost zonally uniform.

Although the standing waves associated with topography are not as effective at localizing the eddy kinetic energy—integration RM has no storm track at all—they appear to be essential for localization of the intraseasonal variability. Integrations 5 and 9 (LSC) stand out from the other integrations in the fact that their annular mode is less localized than the eddy kinetic energy. As noted in section 3, integrations 1, 5, and 9 (LSC) exhibit a stronger north–south dipole in mass than in any of those with topography. They also stand out from the other simulations in terms of their temporal variability (Gerber and Vallis 2007). As discussed therein, the *e*-folding time scale of the annular mode index autocorrelation function provides an indication of the coherence of the annular mode in space (longer time scales result from stronger interactions between the eddies and mean flow). The time scale is 34 days in simulation LSC but just 21 days in RM, 10 days in LSC+RM, and 13 days in LSC+RM2. The stronger feedback leads to higher correlations around the globe. For example, consider the correlation between 40°N, 45°E (a point chosen near the center of the midlatitude lobe of the NAM loading patterns) and points on the opposite side of the globe at the same latitude, between 90° and 180°W. The average correlation is 0.045 (0.26) for the daily (monthly) average SLP for integration LSC

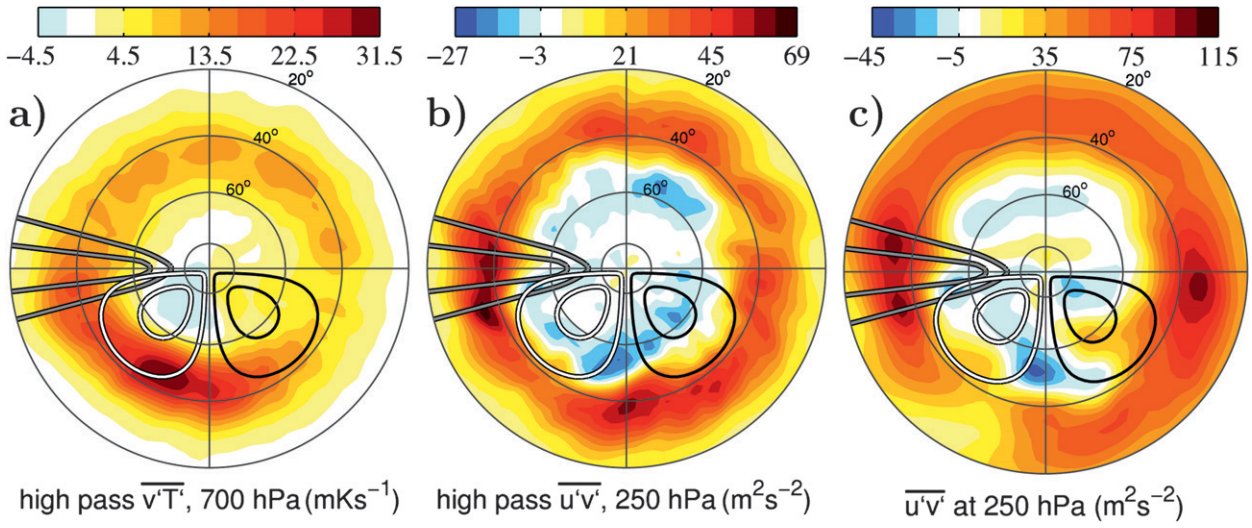

FIG. 8. (a) The 2–10-day eddy heat fluxes, (b) the 2–10-day eddy momentum fluxes, and (c) the total eddy momentum fluxes for integration LSC+RM. The eddy heat flux $\overline{v'T'}$ was computed at 700 hPa, and the momentum flux $\overline{u'v'}$ at 250 hPa.

and 0.030 (0.17) in LSC+RM. Hence, the zonal coherence is 50% higher in integration LSC. This is a conservative estimate; the increase in correlation in LSC becomes more extreme if we consider averages of the correlation between points over wider regions.

The assumption that localized eddy kinetic energy, or eddy stirring, will lead to localized patterns of variability hinges on the assumption that the annular mode is more statistical in nature. By this, we mean that it has a pattern that cannot be interpreted as a teleconnection pattern (Gerber and Vallis 2005). Gerber and Vallis 2005 showed that conservation of momentum (or mass) is sufficient to establish a dominant dipolar pattern, even in the absence of zonally coherent variability. Without zonal coherence, however, moderate localization of the local variability of the jet stream led to significant localization of the NAM pattern (see their Figs. 12 and 13). This is similar to what is observed in integration LSC+RM (and also integrations 8 and 12, not shown), where the NAM is more localized than the EKE.

The presence of underlying coherent flow in the model, as in LSC, will strengthen the annular signal in EOF analysis. In this integration, the annular mode is a more coherent mode of variability, that is, more like a teleconnection pattern, although it should still not be treated as such, given the weak correlation (just 5% on daily time scales) around the globe. The sharp difference in the behavior of the model in cases with realistic stationary wave forcing and cases with uniform or near-uniform forcing (1, 5, and 9) suggests that the latter, with strong eddy–mean flow feedback, is somewhat of a singular limit, fundamentally different from the observed circulation. Topography appears sufficient to limit the eddy–mean flow interactions, moving the model to a more Earth-like regime in which the annular mode cannot be interpreted as a teleconnection (e.g., Ambaum et al. 2001).

5. The NAO and the eddy life cycle

The role of the storm track and eddy–mean flow interactions in setting the zonally asymmetric structure of the NAM suggests that eddies are key to explaining the nonlinear response of the NAM to large-scale forcing. It is known that low-level eddy heat fluxes $v'T'$ are associated with the growing phase of the life cycle (because eddies transfer heat downgradient, tapping energy from the mean flow) and that generally upper-level eddy momentum fluxes $u'v'$ are associated with eddy decay and wave breaking at the end of the life cycle (Simmons and Hoskins 1978). As noted by Swanson (2007), we must be cautious in applying insight from idealized eddy life cycle integrations to the fully nonlinear system because storm tracks cannot be viewed as the simple linear growth and nonlinear breaking of individual eddies. Rather, it is more appropriate to view the storm track as an interaction between the mean flow and eddy wave packets.

We plot the time-averaged eddy heat and momentum fluxes from integration LSC+RM in Fig. 8. Fig. 8a shows the 2–10-day pass filtered eddy heat fluxes. These are maximal in the region poleward of the cooling anomaly, where the large-scale forcing tendency seeks to maximize the temperature gradient. This suggests that baroclinic growth is injecting energy into wave

packets as they pass through this region. We next plot the 2–10-day pass (Fig. 8b) and full eddy momentum fluxes (Fig. 8c). Momentum fluxes reveal regions of wave breaking and hence eddy decay. A strong peak in eddy decay appears above the ridge at all time scales. A second maximum occurs downstream of the baroclinic region as eddies leave the storm track, but here the longitude (and relative strength) of the maximum is sensitive to the temporal scales. The high pass eddies (time scales of 2–10 days) focus attention on synoptic-scale eddies in the storm track. Eddy decay on these time scales reaches a weak maximum near 0°E. As wave packets pass through the difluent region, however, their length and time scales tend to increase (Swanson et al. 1997). This increase in the eddy time scale as the large-scale flow weakens is reflected in the downstream shift to 90°E of the maximum when all time scales are included in the computation the momentum flux.

As in section 4, we can capture the essence of the zonal localization of these processes in a one-dimensional plot by focusing on latitudinal profiles (shown in Fig. 9). We show the localization of the eddy kinetic energy and the NAM on the same plot for comparison. Here we compare the eddy statistics in LSC+RM (forced with both diabatic and thermal perturbations) to the integrations forced by the perturbations separately, LSC and RM. We again show both the high pass and full eddy momentum fluxes to capture the temporal structure of wave breaking in the exit region of the storm track. Figure 9 is a key result of the paper, allowing us to interpret the storm track and the NAO as a spread of the eddy growth and decay in longitude.

Advection by the mean flow distributes the temporal evolution of eddies and wave packets so that in the time average, we can see eddy growth, maturation, and decay spread in longitude over the storm track. Elements of the life cycle are most clear in integrations LSC and LSC+RM. Eddy heat fluxes (baroclinic growth) dominate in the baroclinic region produced by the cold "continent." Eddy energy continues to grow downstream, and the peak EKE occurs some 30° east of the region of peak growth. Eddy momentum fluxes are minimal in the baroclinic region with strong upper-level flow but increase immediately downstream in the difluent region. The time scale of eddy breaking increases further downstream, and the full fluxes exhibit a more well-defined maximum in the region with weakest upper-level flow (where the jet has minimal carrying capacity of wave activity). The NAM tends to follow the structure of the eddy kinetic energy, but inspection of the lower panel in Fig. 9 suggests that the localization of the NAM is shifted slightly downstream of the EKE, biased toward the region of peak eddy momentum fluxes.

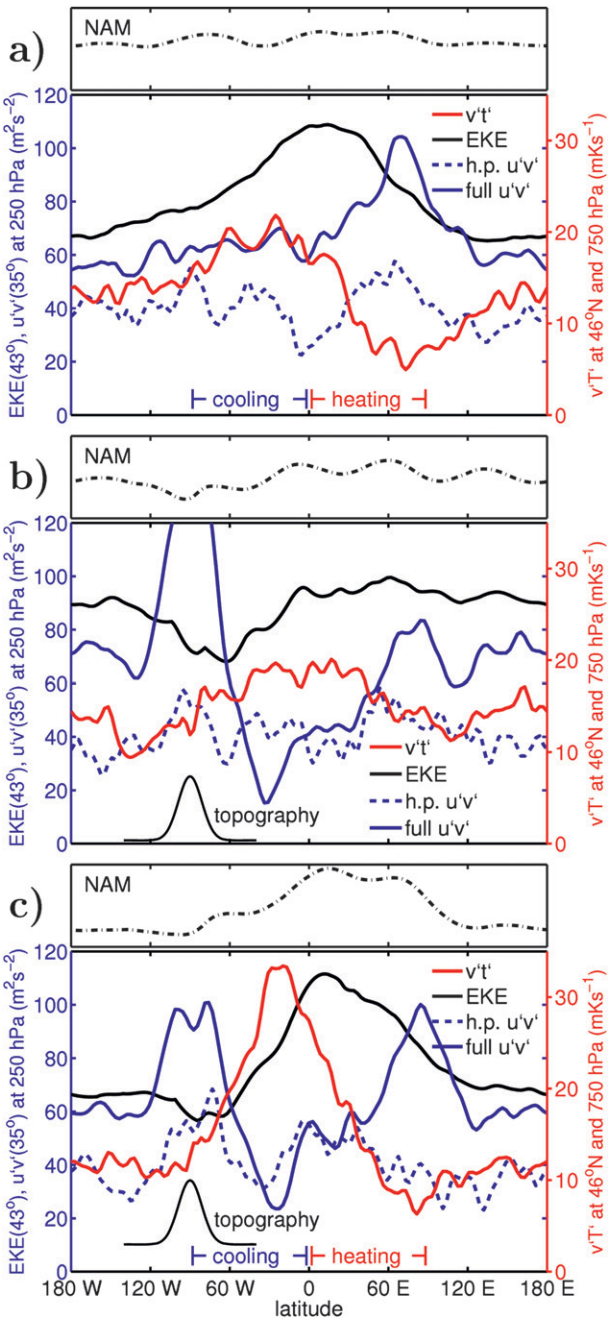

FIG. 9. The storm track, eddy life cycle, and the NAO. Here we plot the heat fluxes (corresponding to the right axes), the EKE and momentum fluxes (corresponding to the left axes), and localization of the NAM pattern as a function of latitude. Statistics are shown from integrations (a) LSC, (b) RM, and (c) LSC+RM. The EKE has been divided by 4 for ease of comparison. The zonal structure of the NAM is computed as described in the appendix.

The peak variability in the NAM begins near the region of increased eddy momentum flux on synoptic time scales and terminates at the peak of the total eddy momentum flux. Eddy heat fluxes in the baroclinic

region redistribute zonal momentum in the vertical by changing the thermal structure of the mean flow but do not affect the meridional distribution of zonal momentum. The variability described by the NAO/NAM is due rather to the eddy momentum fluxes that redistribute momentum north and south. The shift to lower frequencies associated with wave breaking in the difluent region increases power of the NAM on lower frequencies. The zonal spread of the eddy life cycle allows us to refine the notion of ''eddy stirring'' discussed by Vallis et al. [2004, see their Eqs. (2.5)–(2.9)]: the flow may be considered to be primarily stirred by eddy momentum fluxes associated with breaking eddies, not by eddy heat fluxes associated with eddy growth.

The zonal structure of the NAM hence primarily reflects the zonal structure of the storm tracks, but localization of the eddy fluxes alone is clearly not sufficient to produce NAO-like variability. First, in the absence of topography, as in integration LSC, localization of the storm track is not sufficient to strongly localize the variability due to enhanced zonal correlations. Second, strong momentum fluxes over the topography indicate wave breaking over the mountain in both RM and LSC+RM that is not directly associated with the low-frequency variability. Similar wave breaking is observed over the Rocky Mountains in reanalysis observations, as seen in Figs. 10d,e. This may be due to shearing of the eddies by the standing wave generated by the mountain, and there is some indication in the models that the increased transient momentum fluxes may balance the westward torque of the mountain on the mean flow and the PV flux associated with the stationary wave over the mountain (not shown).

The key question, however, is why this wave breaking does not excite low-frequency variability. We speculate that the geometry of the flow is important. Wave breaking over the topography occurs at the entrance to the baroclinic zone where the climatological jet is more baroclinic and chiefly driven by the large-scale forcing. In the exit region of the storm track, the forcing of the baroclinic jet is weak, and momentum fluxes associated with barotropic eddy decay can play a larger role relative to the large-scale forcing. We acknowledge that further study is needed to resolve this question. Wave breaking associated with topography does limit eddy mean flow in the model by preventing eddies from efficiently recycling information around the latitude circle (Gerber and Vallis 2007). This in part explains the weak zonal localization of the NAM in integrations 5 and 9.

6. Analysis of observations

To see if the results we have obtained have parallels in the real world, we analyze the observations in a similar way. We use daily data from 1958 to 2003 on a 2.5° × 2.5° latitude–longitude grid, obtained from a National Centers for Environmental Prediction–National Center for Atmospheric Research (NCEP–NCAR) reanalysis (http://www.cdc.noaa.gov/). Eddies were defined as deviations from the average seasonal cycle, smoothed by a 30-day running mean, and 31 December was omitted from leap years for purposes of constructing the seasonal cycle. Figure 10 shows the baroclinic growth rate, eddy heat fluxes, eddy kinetic energy, eddy momentum fluxes, and annular modes of the atmosphere as found in reanalysis (related plots are shown in Vallis and Gerber 2008). We focus only on the winter months December–February (DJF) for the Northern Hemisphere.

The idealized model integrations capture much of the structure of the eddy and variability fields of the Northern Hemisphere, although in our configuration the model has only one storm track. First note the spread of the eddy life cycle in longitude in both the North Atlantic and Pacific. The strongest baroclinicity, found in the westerly jets off the coasts, is nearly coincident with regions of strong eddy growth. Peak eddy kinetic energy is found downstream of the maximum growth regions and is followed by regions of strong eddy momentum fluxes, particularly in the North Atlantic. As in the model, eddy momentum fluxes shift downstream when all frequencies are considered. The two centers of action of the northern annular mode closely follow that of the eddy kinetic energy, but with a similar downstream bias toward the regions of momentum flux. Thus, in the observations as in the model, the structure of the annular mode follows from the localization of eddy activity in the storm tracks.

Benedict et al. (2004) find that the NAO− phase is associated with cyclonic wave breaking and the NAO+ phase with anticyclonic wave breaking, but the two signs of wave breaking occur in different regions. There is some indication of these preferred breaking regions in the time-mean momentum fluxes. A region of negative $\overline{u'v'}$ off Newfoundland suggests cyclonic breaking. Likewise, positive momentum fluxes dominate in the regions of anticyclonic wave breaking, upstream of the storm track near the Rocky Mountains and downstream in the difluent region extending over North Africa. The model momentum fluxes in Figs. 8b,c show a preference of cyclonic wave breaking $\left(\overline{u'v'} < 0\right)$ north of the jet in the entrance of the difluent region near the prime meridian and greater anticyclonic breaking $\left(\overline{u'v'} > 0\right)$ downstream in the difluent region and upstream over the topography. The Northern Hemispheric fields, however, do differ from the model in other elements. The model does not capture the complexity of wave breaking in the North Atlantic. As seen in Fig. 10e, there are two maxima in the full eddy momentum fluxes, one immediately

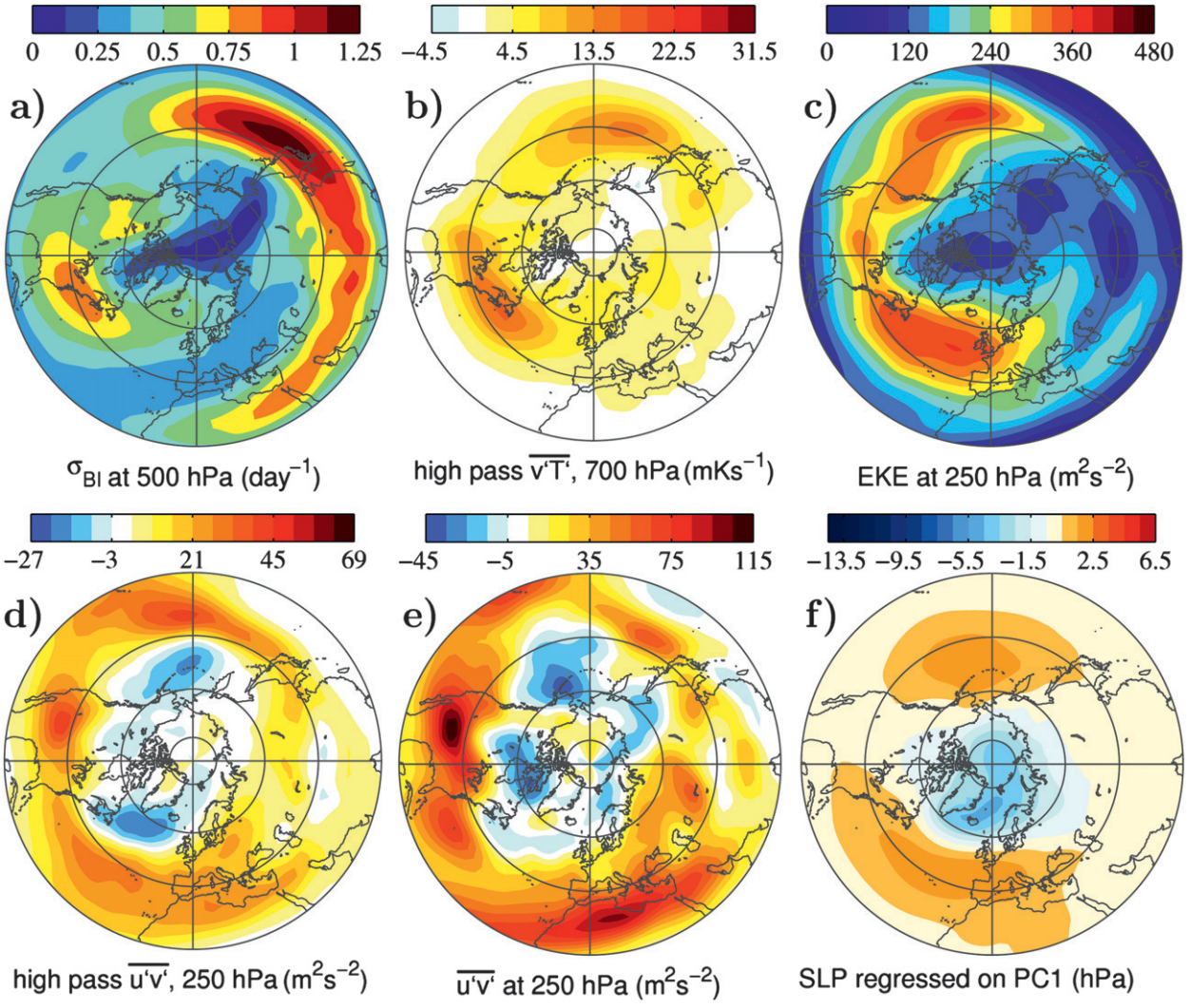

FIG. 10. Evidence of the eddy life cycle in the NH boreal winter (DJF) climatology and its relationship to the NAM. (a) The midtropospheric Eady growth rate, (b) lower-troposphere 2–10-day high-pass eddy heat fluxes, (c) upper-tropospheric kinetic energy, (d) high-pass eddy momentum fluxes, (e) total eddy momentum fluxes, and (f) NAM loading pattern, expressed as an anomaly of SLP. The Eady growth rate σ_{BI} was computed from the winter average climatology at 500 hPa. The eddy heat flux $\overline{v'T'}$ was computed at 700 hPa, and the EKE and momentum fluxes $\overline{u'v'}$ at 250 hPa. The NAM pattern was computed by regressing the daily SLP anomalies on the standardized NAM index. The color scale is the same as that used in the respective plots based on our model integrations.

off the coast of North America, and a second, broader maximum over North Africa. We suspect the large-scale forcing in the model is too simple to capture these features because they may depend on specific details of the coastline and latent heating that are missing in the model.

Stepping back to look at the large-scale circulation, we note that the subtropical jet—the baroclinic flow associated with the strong temperature gradients on the edge of the Hadley cell—in the Northern Hemisphere forms a spiral spanning the entire globe. As seen in Fig. 10a, the baroclinicity, which can be viewed as a proxy for the upper-level flow, begins south and east of the Mediterranean and remains relatively contiguous until fading in the North Pacific. It then reforms over North America, tilting poleward along the east coast, and then vanishing over northern Europe. Viewed in terms of the eddy kinetic energy (Fig. 10c), the Pacific and Atlantic storm tracks appear to merge, with eddy activity remaining high across the gap between jets. [A slightly different viewpoint would be to say that the North Atlantic storm track is very well seeded by the decaying eddy activity left over from the Pacific, so eddies begin at finite amplitude; indeed, there is simply not enough time for an eddy to grow from an infinitesimal size to finite amplitude before being advected out of the Atlantic storm track (Swanson 2007).] Then, all the wave

activity reaches the end of the spiral; the upper-level flow disappears over northern Europe. It is the perfect environment for convergence of eddy kinetic energy, wave breaking, momentum fluxes, and stirring of the mean flow. As demonstrated by our model, this is the recipe for the strong intraseasonal variability, consistent with the peak loading of the NAM in this region, or the localized variability characterized by the NAO.

7. A physical interpretation: Interacting jets

Variability in the Atlantic region of the Northern Hemisphere—the NAO—can be viewed as the interaction of two jets: one subtropical and associated with the meridional temperature gradient at the edge of the Hadley cell; one extratropical and eddy driven. A positive (negative) phase of the NAO corresponds to a splitting (merging) of the jets. However, in the Pacific region, the jet variability cannot be so easily characterized, as noted by Ambaum et al. (2001). Relatedly, Eichelberger and Hartmann (2007) explored the interaction between eddies and the mean flow as a function of the separation between the eddy-driven jet and the subtropical jets. They found greater variability of the eddy-driven flow when there are two distinct jets, as found in the Atlantic. This may be because the subtropical jet is itself usually quite steady, so that when it is merged with the eddy-driven jet, the combination is steadier than the eddy-driven jet alone. Son and Lee (2005) further discuss the dynamics of one and two jet states from a climatological context.

Set against β, the planetary vorticity gradient, the subtropical and extratropical jets appear as anticyclonic/cyclonic perturbations, a kind of one-dimensional vortex pair. Interaction of the jets, depending on the smaller-scale eddy momentum fluxes, can be interpreted as the separation and merger of the vortices, and so of the jets themselves. To describe this more fully we develop a diagnostic of the zonal flow in our model and in reanalysis observations. [This diagnostic was summarized in Vallis and Gerber (2008).] We consider the zonal flow averaged over the each quadrant, separately, so that

$$\bar{u}_j(t,\phi,p) = \frac{2}{\pi}\int_{(j-1)\pi/2}^{j\pi/2} u\,d\lambda, \qquad j = 1,2,3,4. \tag{7.1}$$

With this indexing, the NAM in integration LSC+RM (the integration with NAO-like variability) projects mostly onto the $j = 3$ (and to a lesser extent $j = 2$) quadrants, with the flow averaged from 0° to 90°E and 90°–0°W, respectively, as shown in Fig. 11, where the $\bar{u}_j$ are regressed on the NAM index.

Let us now compare the variability in model winds in these two sectors with the reanalysis winds between 70°W and 20°E (the quadrant with the strongest EOF loading in the observed NAM), and between 160° and 70°W, the quadrant immediately upstream. The quadrant-averaged zonal wind fields are first averaged in 10-day blocks to obtain a smoother signal, $\bar{u}_j^f$. For each block, we then determine the number of maxima in $\bar{u}_j^f(\phi)$ between 10° and 60°N at 250 hPa. (The 60° upper bound was determined empirically; occasionally there are maxima in the winds poleward of this latitude but these are associated with single eddies and so should not be considered a ''jet.'') Examples of one and two jet states taken from the reanalyses are shown in Fig. 12. The percentages of times for which the flow was best classified by one, two, or three jets are shown in Table 4. Upstream of the peak NAM, it is most likely to find only one distinct jet maximum. In the difluent region of peak NAM/NAO variability, however, it is most likely to find two distinct jets.

Focusing now on the peak NAM/NAO region, we make the criterion stricter for there to be two distinct jets. We say that the two jets are ''strongly separated'' if the minimum winds between them are an amount m or more (in m s^{-1}) weaker than both of the two maxima. The values $m = 9.6$ m s^{-1} and $m = 4.2$ m s^{-1}, for observations and model, respectively, were chosen empirically so that there are equally many cases of well-separated double jets and single jets, as shown in Table 5. Two ''weakly separated'' jets exhibit two distinct maxima in the upper-level winds but do not satisfy the strongly separated criterion. To illustrate these criteria, Fig. 12 shows a single-jet case and a strongly separated two-jet case, with maximum winds at 250 hPa of 39 and 29 m s^{-1} near 20° and 50°N, respectively. The minimum winds between these two points are only 9 m s^{-1}, so the depth of the minimum is 20 m s^{-1}, more than twice the amount required to satisfy the criterion set by $m = 9.6$ m s^{-1}.

We have thus classified all instances of the jet in the peak NAM/NAO quadrant into one of three bins: one jet, two weakly separated jets, or two well-separated jets, with each bin holding approximately one-third of the cases. (In instances of three jets, we look at the separation between the two jets closer to the equator because these best characterize the subtropical and extratropical jets.) We now form composites of the jet from these three bins and then compare them to averages of the jet based on the annular mode index. In forming composites from the annular mode index, we divide the same dataset into three groups: negative states, in which the index is below $-c$, neutral states, in which it is between $-c$ and c, and positive states, in

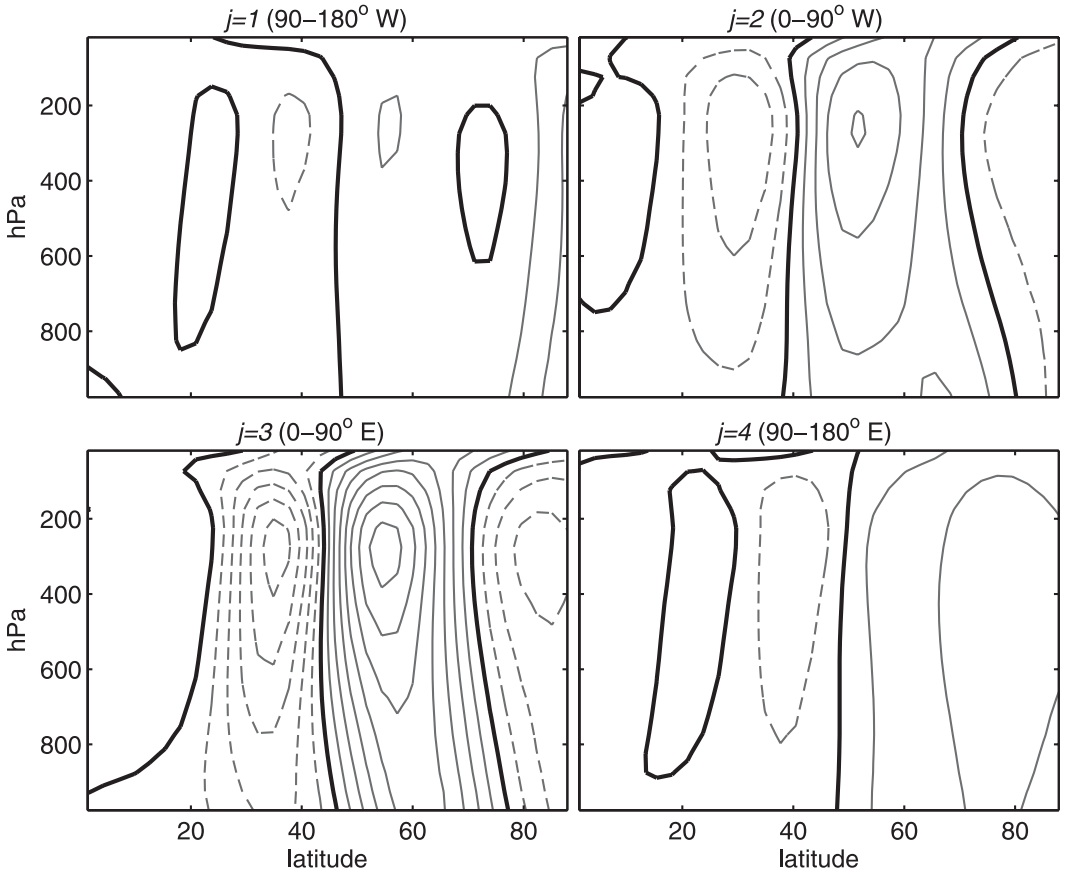

FIG. 11. The quadrant-averaged zonal wind $\bar{u}_j$ regressed onto the NAM index for quadrants $j = 1, 2, 3$, and 4, respectively, for model integration LSC+RM.

which it is above c. The value of the cutoff, $c = 0.42$, was chosen to similarly partition the time series as in our one/two jet measure. We note that the annular mode index is skewed with a longer tail on negative side so that there are slightly more events in the positive bin.

As illustrated in Fig. 13, the partition based on the state of the jet (one jet versus a split jet), provides the same information as the partition based on the annular mode index, as is also apparent from Figs. 6a and 6b of Ambaum et al. (2001). This observation suggests a more physical characterization of the NAM. In a high index state, the eddy-driven jet is well separated from the subtropical jet: there are two well-separated vortex pairs. In the low index state, the two jets have merged, leaving only one pair. Such transitions occur mainly in the quadrant where eddy momentum fluxes are large and the subtropical flow is weak, allowing the extratropical jet to separate. In this context, the NAO can be viewed as the separation and merger of the jets, although the geophysical fluid dynamics of this problem needs to be more fully elucidated.

8. Summary and conclusions

We have investigated the influence of large-scale topographic and thermal forcing on the zonal structure of the synoptic storm tracks and patterns of intraseasonal variability in a dry primitive equation model. Standing waves are generated with a Gaussian ridge similar in scale to the Rocky Mountains and diabatic heating anomalies that approximate cooling and warming over a continent and ocean during the winter season. Although we find the stationary wave response to be a roughly linear function of the topography and thermal forcing, the storm tracks and the associated patterns of variability are not. By varying the amplitude and structure of the standing waves, we found a range of storm tracks and patterns of intraseasonal variability, from ideal annular modes to well-localized NAO-like structures.

We have extended and critiqued the hypothesis that the zonal structure of the patterns of intraseasonal variability essentially follows from that of the underlying synoptic variability. Given that the NAM is largely forced by synoptic eddies and standing waves, can its

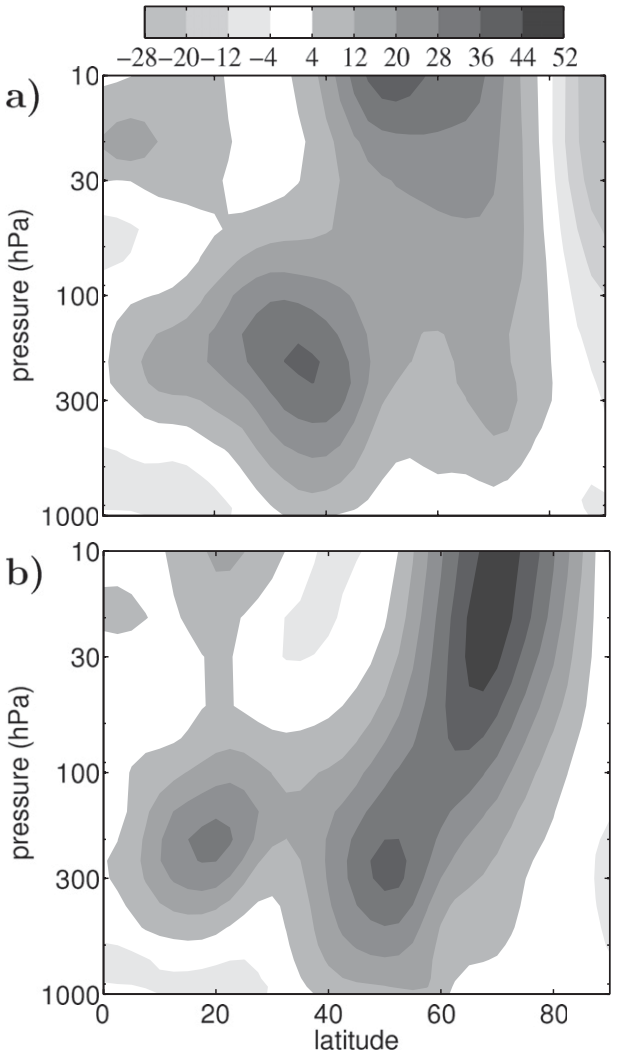

FIG. 12. Sample (a) one- and (b) two-jet cases found for the 70°W–20°E average zonal wind, using NCEP–NCAR reanalysis winds. The winds in (a) come from mid-January 1985. The winds in (b) are from late January 1990.

structure be deduced simply from those of the eddy statistics? We find that this heuristic holds to some degree but that patterns established by EOF analysis are extremely sensitive to the underlying forcing, and the response is nonlinear with respect to different combinations of stationary waves. NAO-like variability in our model comes about when the standing waves generated by the topography and diabatic forcing are combined and aligned; here the first EOF became much more localized compared with the localization of the variability responding to topography or diabatic heating alone. A 30° shift of the topography relative to the diabatic forcing, however, breaks this interaction, and the variability can be more easily related to that of the two components separately.

TABLE 4. Classification of $\bar{u}_j^f$ flow into one, two, or three jet states. We classify the flow into cases with one, two, or three jets for the regions leading to the entrance to the storm track (160°–70°W in the reanalysis and 90°W–0° in the model) and for the regions in the peak NAM/NAO loading (70°W–20°E in the reanalysis and 0°–90°E in the model). In both model and observations a split jet is more favored in the NAO region.

	% cases with n jets		
Quadrant	1	2	3
Observations 160°–70°W	57.2	40.8	1.9
Observations 70°W–20°E	31.4	64.0	4.6
Model 90°W–0°	75.1	24.9	0
Model 0°–90°E	31.8	67.4	0.8

We also find that EOF analysis is very sensitive to the strength of eddy–mean flow feedback in the model. Localization of the intraseasonal variability requires both localization of the synoptic storm track and disruption of coherent hemispheric variability. Although topographic stationary waves do not appear to be as effective at organizing the structure of the storm track as the diabatic perturbations, they appear to be critical for localizing the low-frequency variability as they limit eddy mean–flow interactions.

We began our discussion with three questions. Let us now address these in light of our model integrations and observations from reanalysis data.

1) *What are the key features of the thermal and orographic induced stationary wave patterns that give rise to a synoptic storm track?*

   We find that localization of baroclinic instability alone is not sufficient for localization of the eddy kinetic energy, consistent with more theoretical studies (e.g., Pierrehumbert 1984; Chang and Orlanski 1993; Swanson et al. 1997). A key ingredient for a zonally

TABLE 5. Different criteria for classifying the quadrant-average zonal wind in the peak NAM region (70°W to 20°E in reanalysis and 0°–90°E in the model). The distinction between weakly separated and strongly separated jets is discussed in the text. Low and high index NAM events are classified as instances when the annular mode index dips below (rises above) −(+)0.42 std dev.

	% cases	
Criteria	Observations	Model
One distinct jet	31.4	31.8
Two weakly separated jets	37.2	36.4
Two strongly separated jets	31.4	31.8
Low NAM	30.4	30.8
Neutral NAM	36.7	36.1
High NAM	32.9	33.1

[1]Some results from integrations 1, 9, 11, and 13 were presented in abbreviated form in a review paper by Vallis and Gerber (2008). Because of differing publication schedules, that material appeared in print before this paper.

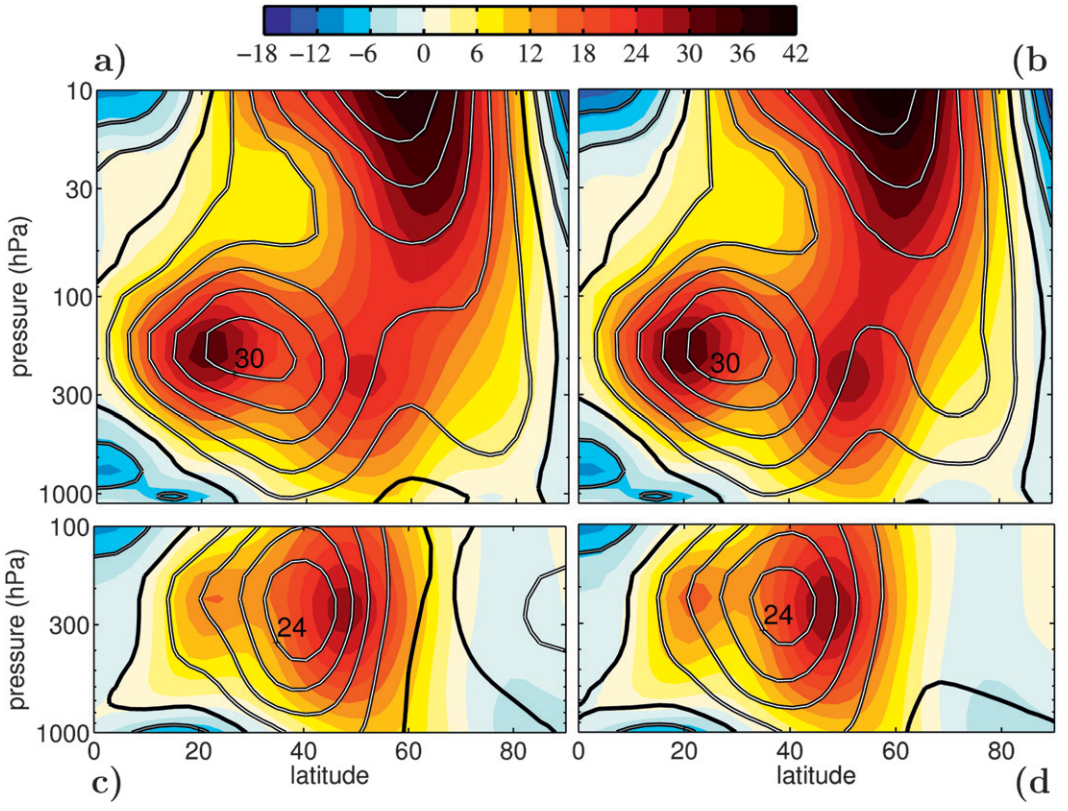

FIG. 13. Jet composites of the zonal winds based on (a),(c) the NAM index and (b),(d) jet separation analysis. We find that the jet separation analysis provides the same information as composites based on the NAM index for both the (a),(b) reanalyses and (c),(d) model winds. The contours illustrate composites based on cases in which the NAM index is low on the left and in which there is just one distinct jet on the right. Shading illustrates composites based on times when the NAM index is high on the left and there are two well-separated jets on the right. The winds are averaged in just the quadrant with peak NAM/NAO loading: between 70°W and 20°E for reanalyses and between 0° and 90°E for model output.

localized storm track appears to be a difluent region of weak upper-level flow that forces eddies to break, thus preventing the downstream propagation of eddy energy. The diabatic (land–sea contrast) perturbation in our model was most effective at creating this minimum in the upper-level flow and thus at creating a localized storm track. In the atmosphere, the weakest upper-level flow is found at the end of the spiraling subtropical jet over the eastern Atlantic Ocean and northern Europe. It is here that the North Atlantic storm track begins to decay; indeed, to some degree it is here that the ''Northern Hemisphere storm track'' begins to decay, because by some measures the Pacific storm track never really dies over North America.

2) *How does the life cycle of an eddy—or, rather, the evolution of an eddy wave packet—in a zonally varying flow relate to the large-scale variability?*

We find evidence of different states of the eddy life cycle spread out in longitude by winds advecting individual eddies and wave packets through the storm tracks, both in our model and in the Northern Hemisphere. In Fig. 14, we sketch out the relationship between the mean flow and eddy activity. Eddy growth is largest in baroclinic regions of strong temperature gradients (and thus upper-level flow). Eddies continue to grow as they leave the most unstable region, and the eddy kinetic energy does not begin to decline until the upper-level flow weakens, forcing waves to break.

The intraseasonal variability connects to eddy evolution through the momentum fluxes associated with wave breaking and dissipation at the end of the life cycle. It is in these regions that the eddies are stirring the barotropic circulation, reorganizing momentum. Marked localization of the variability, however, appears also to depend on the nature of zonal eddy feedback in the model, as observed by the weak localization in integrations without topography. Localization of the eddy forcing is a necessary but not sufficient condition for localizing the intraseasonal variability.

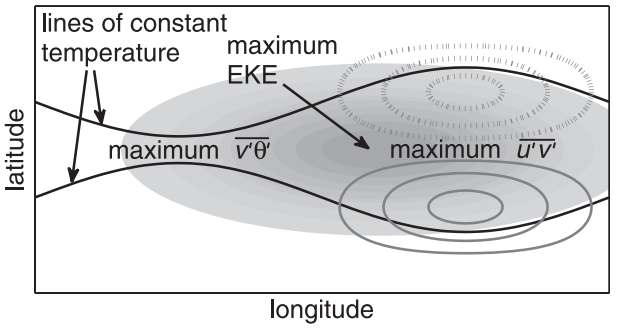

FIG. 14. A diagram illustrating the relationship between intraseasonal variability (the dipole pattern shown with solid and dashed gray contours), the baroclinicity of the flow (as inferred from the black contours of temperature), and the eddy statistics. Eddy growth dominates in the baroclinic regions, but eddies continue to grow as they are advected downstream. Downstream development tends to maintain the eddy kinetic energy despite variation in the growth rates. Most critical is a difluent region in which the weak upper-level flow cannot support as many waves and wave breaking and dissipation begin to dominate, producing eddy momentum fluxes. Intraseasonal variability is the response to this stirring of the large-scale flow by eddies.

We acknowledge, however, that this interpretation may oversimplify the details of cyclonic and anticyclonic wave breaking in the observed NAO (e.g., Benedict et al. 2004). This idealized view leaves out many critical features in the atmospheric circulation. Cyclonic wave breaking tends to occur on the upstream end of the difluent region and may depend more critically on the slope of the North Atlantic coastline and latent and sensible heating associated with strong cyclones. The lack of variability in the Pacific storm track, which is much more baroclinic, may be due to the fact that the eddies do not have enough time to grow before being advected out of the growth region. Furthermore, the Atlantic storm track is much more well seeded: disturbances enter the baroclinic region at finite amplitude and have more time to interact with the weaker flow.

3) *How is the presence of a zonally localized storm track related to, or even the same as, the NAO?*

We have shown that a zonally localized storm track depends on wave breaking and dissipation, processes that prevent downstream development. These processes also transfer energy to the mean flow, stirring the zonal momentum. Localized synoptic variability and enhanced variability of the extratropical jet as it splits and merges with the subtropical jet—the NAO—are two manifestations of the same underlying phenomena. Thus, variability in the NAO does not cause the storm track to shift; rather, it is a signal of the shift.

Acknowledgments. The authors thank three anonymous reviewers for insightful comments on an early version of the manuscript, Dr. Paul Kushner for helpful discussions, and Dr. David Thompson for kindly providing the NAM and SAM loading patterns. The work was partially funded by the National Science Foundation, and EPG also thanks the Fannie and John Hertz Foundation for support.

APPENDIX

Quantifying the Zonal Asymmetry of the NAM

The annular modes are defined by the first empirical orthogonal function of the 25-day average sea level pressure. The modes chiefly describe a vacillation of the barotropic, extratropical jet, so we quantify the localization of the pattern in longitude based on the reorganization of angular momentum associated with the mode. Because the patterns have little net angular momentum, we use the absolute value at each latitude:

$$\mathrm{NAM}(\lambda) = \alpha \int_0^{\pi/2} \left\| -\frac{d\psi}{d\phi} \right\| \cos^2 \phi \, d\phi. \qquad \text{(A.1)}$$

The constant α is used to scale the momentum reorganization so that its maximum across all integrations is unity. (The maximum is found in integration LSC+RM.)

REFERENCES

Ambaum, M. H. P., B. J. Hoskins, and D. B. Stephenson, 2001: Arctic Oscillation or North Atlantic Oscillation? *J. Climate,* **14,** 3495–3507.

Benedict, J. J., S. Lee, and S. B. Feldstein, 2004: Synoptic view of the North Atlantic Oscillation. *J. Atmos. Sci.,* **61,** 121–144.

Cash, B. A., P. Kushner, and G. K. Vallis, 2005: Zonal asymmetries, teleconnections, and annular patterns in a GCM. *J. Atmos. Sci.,* **62,** 207–219.

Chang, E. K. M., and I. Orlanski, 1993: On the dynamics of a storm track. *J. Atmos. Sci.,* **50,** 999–1015.

DeWeaver, E., and S. Nigam, 2000: Zonal-eddy dynamics of the North Atlantic Oscillation. *J. Climate,* **13,** 3893–3914.

Duchon, C. E., 1979: Lanczos filtering in one and two dimensions. *J. Appl. Meteor.,* **18,** 1016–1022.

Eichelberger, S. J., and D. L. Hartmann, 2007: Zonal jet structure and the leading mode of variability. *J. Climate,* **20,** 5149–5163.

Feldstein, S. B., 2000a: Is interannual zonal mean flow variability simply climate noise? *J. Climate,* **13,** 2356–2362.

——, 2000b: The timescale, power spectra, and climate noise properties of teleconnection patterns. *J. Climate,* **13,** 4430–4440.

Gerber, E. P., and G. K. Vallis, 2005: A stochastic model for the spatial structure of annular patterns of variability and the NAO. *J. Climate,* **18,** 2102–2118.

——, and ——, 2007: Eddy-zonal flow interactions and the persistence of the zonal index. *J. Atmos. Sci.,* **64,** 3296–3311.

——, S. Voronin, and L. M. Polvani, 2008: Testing the annular mode autocorrelation time scale in simple atmospheric general circulation models. *Mon. Wea. Rev.,* **136,** 1523–1536.

Held, I. M., and M. J. Suarez, 1994: A proposal for the intercomparison of the dynamical cores of Atmospheric General Circulation Models. *Bull. Amer. Meteor. Soc.,* **75,** 1825–1830.

Hoskins, B. J., and P. J. Valdes, 1990: On the existence of storm-tracks. *J. Atmos. Sci.,* **47,** 1854–1864.

Jin, F.-F., L.-L. Pan, and M. Watanabe, 2006: Dynamics of synoptic eddy and low-frequency flow interaction. Part I: A linear closure. *J. Atmos. Sci.,* **63,** 1677–1694.

Lee, S., 1995: Localized storm tracks in the absence of local instability. *J. Atmos. Sci.,* **52,** 977–989.

Limpasuvan, V., and D. L. Hartmann, 2000: Wave-maintained annular modes of climate variability. *J. Climate,* **13,** 4414–4429.

North, G. R., T. L. Bell, R. F. Cahalan, and F. J. Moeng, 1982: Sampling errors in the estimation of empirical orthogonal functions. *Mon. Wea. Rev.,* **110,** 699–706.

Pierrehumbert, R. T., 1984: Local and global baroclinic instability of zonally varying flow. *J. Atmos. Sci.,* **41,** 2141–2162.

Simmons, A., and B. Hoskins, 1978: The life cycles of some nonlinear baroclinic waves. *J. Atmos. Sci.,* **35,** 414–432.

Son, S.-W., and S. Lee, 2005: The response of westerly jets to thermal driving in a primitive equation model. *J. Atmos. Sci.,* **62,** 3741–3757.

Swanson, K. L., 2007: Storm track dynamics. *The Global Circulation of the Atmosphere,* T. Schneider and A. H. Sobel, Eds., Princeton University Press, 78–103.

——, P. J. Kushner, and I. M. Held, 1997: Dynamics of barotropic storm tracks. *J. Atmos. Sci.,* **54,** 791–810.

Vallis, G. K., 2006: *Atmospheric and Oceanic Fluid Dynamics: Fundamentals and Large-Scale Circulation*. Cambridge University Press, 745 pp.

——, and E. P. Gerber, 2008: Local and hemispheric dynamics of the North Atlantic Oscillation, annular patterns, and the zonal index. *Dyn. Atmos. Oceans,* **44,** 184–212.

——, ——, P. J. Kushner, and B. A. Cash, 2004: A mechanism and simple dynamical model of the North Atlantic Oscillation and annular modes. *J. Atmos. Sci.,* **61,** 264–280.

Whitaker, J. S., and R. M. Dole, 1995: Organization of storm tracks in zonally varying flows. *J. Atmos. Sci.,* **52,** 1178–1191.

Woollings, T. J., and B. J. Hoskins, 2008: Simultaneous Atlantic–Pacific blocking and the northern annular mode. *Quart. J. Roy. Meteor. Soc.,* **134,** 1635–1646.